Dichotomous Exciton Conversion at a DPP2Py2T-PCBM interface: Insights from embedded GW-Bethe–Salpeter Equation calculations

Vivek Sundaram[†,‡,¶] and Björn Baumeier[*,†,‡]

†*Department of Mathematics and Computer Science, Eindhoven University of Technology, P.O. Box 513, 5600MB Eindhoven, The Netherlands*

‡*Institute for Complex Molecular Systems, Eindhoven University of Technology, P.O. Box 513, 5600MB Eindhoven, The Netherlands*

¶*Department of Applied Physics and Science Education, Eindhoven University of Technology, P.O. Box 513, 5600MB Eindhoven, The Netherlands*

E-mail: b.baumeier@tue.nl

Abstract

Depending on the initial photoexcitation of the donor or acceptor phase, different efficiencies of charge generation can be observed in organic solar cells. We investigate the origin of this dichotomy by simulations based on quantum–quantum–classical embedded *GW*–Bethe–Salpeter equation of conversion dynamics from localized to charge-transfer (CT) excitations at the interface of a diketopyrrolopyrrole (DPP) polymer and fullerene. Specifically, we determine the excitonic energy levels, their electronic couplings, and the reorganization energies for the respective conversion processes within Marcus theory. Our calculations yield a variety of CT-type excitations of different characters with the lowest integer CT excitations of relevance for charge generation separated by 0.30 eV. Further analysis reveals that the activation barrier for conversion to the lowest CT state is significantly higher (0.25 eV) for the polymer LE than for the fullerene LE (0.05 eV), leading to a preferred population of the higher, less strongly bound CT state from the photoexcited donor. From a population dynamics model we find that, indeed, on the time scale of one picosecond after the respective excitation, the donor excitation leads to the formation of a CT excitation with on average 0.16-0.27 eV lower electron-hole binding energy, providing a pathway to faster charge separation.

TOC Graphic

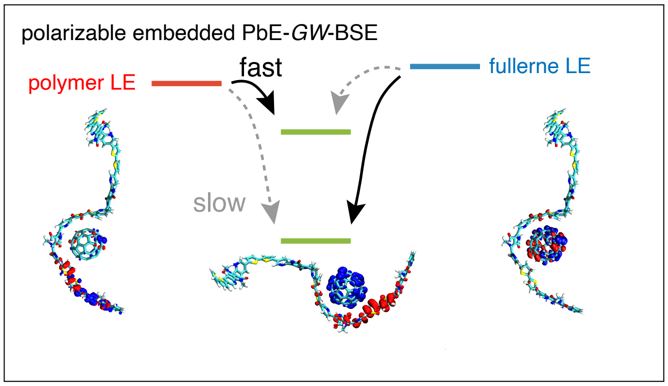

Introduction

Organic photovoltaic devices convert solar energy into electricity through a series of fundamental processes: light absorption, exciton generation, charge separation at donor-acceptor interfaces, and charge collection. In bulk heterojunction solar cells, both the polymer donor and fullerene acceptor can absorb light and generate excitons, which then migrate to the interface where they may form interfacial charge-transfer (CT) states as precursor state for charge generation. The efficiency of charge generation thus depends critically on the energetics and dynamics of exciton conversion across the heterojunction[1,2].

Among the intensively studied donor-acceptor materials are oligomers based on diketopyrrolopyrroles (DPP) for donors and fullerene (C_{60}) based compounds (PCBM) for acceptors[3–5]. They can be easily modified by adding various aromatic and π-conjugated substituents to the backbone and different side chains to DPP, affecting both the solubility and crystallinity of the polymer and its electronic properties. With suitable substituents, a low band-gap internal donor-acceptor architecture leads to efficient harvesting of the solar energy spectrum and a power conversion efficiency (PCE) of around 8 % in blends with fullerene acceptors[6–9].

While it is commonly assumed that charge generation via donor or acceptor excitation proceeds with similar efficiency, recent experiments have shown that this assumption often fails. In particular, Hendriks et al.[10] demonstrated a dichotomous behavior in DPP polymer-fullerene solar cells: efficient charge separation via acceptor excitation (hole transfer) requires a driving force ∼0.3 eV larger than that required for donor excitation (electron transfer)[10]. By comparing external quantum efficiency (EQE) spectra across 16 polymer-fullerene blends, they revealed that the minimum energy needed to drive charge generation from fullerene excitons is significantly higher than for polymer excitons. These results suggest the existence of distinct energy barriers and possibly different kinetic mechanisms for donor- and acceptor-initiated charge separation.

Understanding the microscopic origin of this asymmetry demands a theoretical framework that captures both the energetics of CT state formation and the kinetic barriers for exciton conversion. Marcus theory provides a basis for describing such processes, accounting for the electronic coupling between initial and final states as well as the reorganization energies of donor and acceptor[11–13]. However, a fully quantum mechanical treatment of exciton conversion at complex donor-acceptor interfaces has remained challenging due to the computational demands of accurate excited-state methods.

Recent progress in embedding techniques has begun to address this challenge. Subsystem time-dependent density functional theory (TDDFT), including frozen-density embedding and QM/MM-TDDFT, has been applied to simulate localized excitations in solvated chromophores and biological complexes, providing a computationally efficient approach to model environmental effects on excited states[14,15]. Yet, TDDFT-based methods can struggle with long-range charge-transfer excitations and double excitation character, which are often central to interfacial CT processes.

In contrast, embedding schemes based on many-body Green's function theory employing the GW approximation and the Bethe–Salpeter equation (GW-BSE) offer an alternative to TDDFT with a more rigorous treatment of quasiparticle and excitonic effects[16,17]. Embedding techniques such as projection-based quantum-quantum-classical embedding[18,19], local orbital truncation[20], and polarizable continuum models[21,22] have recently made GW-BSE calculations tractable for systems of several hundred atoms. These methods preserve the accuracy of many-body approaches while incorporating environmental effects at lower computational cost, enabling simulations of realistic interfaces in molecular materials and nanostructures[23].

Here, we employ a quantum-quantum-classical (QM/QM/MM) projection-based embedded GW-BSE (PbE-GW-BSE) approach[18,19] to investigate exciton conversion dynamics at a DPP2Py2T-PCBM interface, a high-performing system in the series studied by Hendriks et al.[10] which has experimentally shown the dichotomous role of donor or acceptor excitation in the charge generation process. A representative bulk heterojunction structure is chosen from a previously simulated interface[24]. The morphology of this interface had been obtained from classical molecular dynamics (MD) simulations mimicking explicit solvent evaporation. Not only do we push the limits of accessible system sizes for GW-BSE calculations, but we also compute all parameters (energies of localized and CT excitations, their electronic couplings, and reorganization energies) required to set up a kinetic model. Focusing in particular on the conversion from initially excited localized excitations in DPP2Py2T or PCBM[60] to bimolecular charge transfer excitations, it is attractive to consider them by an effective transfer rate[25–27]. In the non-adiabatic high temperature or activated crossing limit, Marcus theory[12,28] yields the rate of electronic excitation transfer between an initial LE and final CT state as

$$\omega_{\text{LE-CT}} = \frac{2\pi}{\hbar} \frac{|J_{\text{LE-CT}}|^2}{\sqrt{4\pi\lambda_{\text{LE-CT}} k_{\text{B}} T}} \exp\left[-\frac{(\Delta E_{\text{LE-CT}} - \lambda_{\text{LE-CT}})^2}{4\lambda_{\text{LE-CT}} k_{\text{B}} T}\right], \tag{1}$$

where $\Delta E_{\text{LE-CT}}$ is the adiabatic energy difference, and $\lambda_{\text{LE-CT}}$ the reorganization energy. The expression also contains the *non-adiabatic coupling* element, $J_{\text{LE-CT}}$.

Using the such calculated rates in a kinetic model allows us to elucidate for the first time the distinct pathways and energy barriers for exciton conversion depending on whether the initial excitation occurs in the donor or acceptor phase. Our calculations reveal a dichotomous behavior in the accessibility of CT states depending on the initially excited component and provide a microscopic rationale for the observed asymmetry in charge generation. Crucially, the technical developments in quantum-quantum-classical embedding are what make such a study on this scale possible.

In the following, we will first briefly recapitulate the methodology of projection-based embedded GW-BSE calculations. Then we focus on simulating and analyzing the excitonic processes at the DPP2Py2T-PCBM interface, starting with the characterization and identification of relevant localized and CT excitations in vacuum and with polarizable embedding. This is followed by estimates of reorganization energies as well as non-adiabatic excitonic couplings. Finally, we employ these parameters in a kinetic model to simulate the population dynamics and elucidate the dichotomous exciton conversion pathways.

Projection-based embedded GW-BSE calculations

Within the framework of perturbation theory with many-body Green's functions, one first obtains wavefunctions $\phi_i^{\mathrm{KS}}(\mathbf{r})$ and energies $\varepsilon_i^{\mathrm{KS}}$ from Kohn–Sham (KS) DFT[29]

$$\left\{-\frac{1}{2}\Delta + v_{\mathrm{ext}}(\mathbf{r}) + v_{\mathrm{H}}(\mathbf{r}) + v_{\mathrm{xc}}(\mathbf{r})\right\}\phi_i^{\mathrm{KS}}(\mathbf{r}) = \varepsilon_i^{\mathrm{KS}}\phi_i^{\mathrm{KS}}(\mathbf{r}), \tag{2}$$

where v_{ext} is the external potential, v_{H} the Hartree potential, and v_{xc} the exchange-correlation potential. In the GW approximation[30,31] and under the assumption that the "true" quasiparticle QP wave functions $\phi_i^{\mathrm{QP}}(\mathbf{r})$ are well approximated by the KS wave functions, the QP energies can be obtained perturbatively by evaluating

$$\varepsilon_i^{\mathrm{QP}} = \varepsilon_i^{\mathrm{KS}} + \left\langle \phi_i^{\mathrm{KS}} \middle| \Sigma(\varepsilon_i^{\mathrm{QP}}) - v_{\mathrm{xc}} \middle| \phi_i^{\mathrm{KS}} \right\rangle. \tag{3}$$

The self-energy $\Sigma = \mathrm{i}GW$ is calculated in frequency space (with $\eta \to 0^+$ to ensure convergence) as

$$\Sigma(\mathbf{r},\mathbf{r}',\omega) = \frac{\mathrm{i}}{2\pi}\int G(\mathbf{r},\mathbf{r}',\omega+\omega')W(\mathbf{r},\mathbf{r}',\omega')e^{\mathrm{i}\omega'\eta}\,d\omega', \tag{4}$$

from the Green's function based on the Kohn–Sham solution

$$G(\mathbf{r},\mathbf{r}',\omega) = \sum_m \frac{\phi_m^{\mathrm{KS}}(\mathbf{r})\phi_m^{\mathrm{KS}*}(\mathbf{r}')}{\omega - \varepsilon_m^{\mathrm{KS}} - \mathrm{i}\eta\,\mathrm{sgn}(E_{\mathrm{F}} - \varepsilon_m^{\mathrm{KS}})} \tag{5}$$

and the screened Coulomb interaction W in the random phase approximation.

$$W(\mathbf{r},\mathbf{r}',\omega) = \int \epsilon^{-1}(\mathbf{r},\mathbf{r}'',\omega)v_{\mathrm{C}}(\mathbf{r}'',\mathbf{r}')\,d^3r''. \tag{6}$$

The evaluation of Eq. (6) in turn requires the microscopic frequency-dependent dielectric function given by

$$\epsilon(\mathbf{r},\mathbf{r}',\omega) = \delta(\mathbf{r},\mathbf{r}') - \int v_{\mathrm{C}}(\mathbf{r},\mathbf{r}'')\chi_0(\mathbf{r}'',\mathbf{r}',\omega)\,d^3r'' \tag{7}$$

containing the irreducible polarizability χ_0:

$$\chi_0(\mathbf{r},\mathbf{r}',\omega) = \sum_v^{\text{occ}} \sum_c^{\text{unocc}} \left\{ \frac{\phi_v^{\text{KS}*}(\mathbf{r})\phi_c^{\text{KS}}(\mathbf{r})\phi_c^{\text{KS}*}(\mathbf{r}')\phi_v^{\text{KS}}(\mathbf{r}')}{\omega - (\varepsilon_c^{\text{KS}} - \varepsilon_v^{\text{KS}}) + \mathrm{i}\eta} \right. \\ \left. - \frac{\phi_v^{\text{KS}}(\mathbf{r})\phi_c^{\text{KS}*}(\mathbf{r})\phi_c^{\text{KS}}(\mathbf{r}')\phi_v^{\text{KS}*}(\mathbf{r}')}{\omega + (\varepsilon_c^{\text{KS}} - \varepsilon_v^{\text{KS}}) - \mathrm{i}\eta} \right\}. \tag{8}$$

The structure of Eq. (7) allows to separate the full self energy into an explicitly frequency-dependent correlation part

$$\Sigma^{\text{c}}(\mathbf{r},\mathbf{r}',\omega) = \frac{\mathrm{i}}{2\pi} \int G(\mathbf{r},\mathbf{r}',\omega+\omega') \left(W(\mathbf{r},\mathbf{r}',\omega') - v_{\text{C}}(\mathbf{r},\mathbf{r}')\right) d\omega'. \tag{9}$$

and a bare exchange part

$$\begin{aligned} \Sigma^{\text{x}}(\mathbf{r},\mathbf{r}') &= \frac{\mathrm{i}}{2\pi} \int G(\mathbf{r},\mathbf{r}',\omega+\omega') v_{\text{C}}(\mathbf{r},\mathbf{r}') e^{\mathrm{i}\omega'\eta}\, d\omega' \\ &= -\sum_v^{\text{occ}} \phi_v^{\text{KS}}(\mathbf{r})\phi_v^{\text{KS}*}(\mathbf{r}') v_{\text{C}}(\mathbf{r},\mathbf{r}'). \end{aligned} \tag{10}$$

Eq. (3) can be rewritten into the fixed-point problem

$$\omega - \omega_i = \Sigma_i^{\text{c}}(\omega), \tag{11}$$

with $\omega_i = \varepsilon_i^{\text{KS}} + \langle\phi_i^{\text{KS}}|\, \Sigma^{\text{x}} - v^{\text{KS}}\, |\phi_i^{\text{KS}}\rangle$ and $\langle\phi_i^{\text{KS}}|\, \Sigma^{\text{c}}(\omega)\, |\phi_i^{\text{KS}}\rangle = \Sigma_i^{\text{c}}(\omega)$.

The *Bethe–Salpeter equation* (BSE), $\underline{\mathbf{H}}^{\text{BSE}}\, |\zeta_S\rangle = \Omega_S\, |\zeta_S\rangle$, extends the quasiparticle picture to charge-neutral excitations that involve excitonic effects (electron-hole pair interaction) in a two-particle excitation. Here, the electron-hole wave functions $|\zeta_S\rangle$ are typically expressed in a basis of resonant and antiresonant products of single-particle functions

$$\zeta_S(\mathbf{r},\mathbf{r}') = \sum_v^{\text{occ}} \sum_c^{virt} A_{vc}^S \phi_c(\mathbf{r})\phi_v^*(\mathbf{r}') + B_{vc}^S \phi_v(\mathbf{r})\phi_c^*(\mathbf{r}'). \tag{12}$$

With that, the BSE explicitly reads in matrix form

$$\begin{pmatrix} \underline{\mathbf{H}}^{\text{res}} & \underline{\mathbf{K}} \\ -\underline{\mathbf{K}} & -\underline{\mathbf{H}}^{\text{res}} \end{pmatrix} \begin{pmatrix} \mathbf{A}^S \\ \mathbf{B}^S \end{pmatrix} = \Omega_S \begin{pmatrix} \mathbf{A}^S \\ \mathbf{B}^S \end{pmatrix}, \tag{13}$$

with elements

$$H^{\text{res}}_{vc,v'c'}(\omega) = D_{vc,v'c'} + K^{\text{x}}_{vc,v'c'} + K^{\text{d}}_{vc,v'c'} \tag{14}$$

$$K_{cv,v'c'}(\omega) = K^{\text{x}}_{cv,v'c'} + K^{\text{d}}_{cv,v'c'}. \tag{15}$$

and

$$D_{vc,v'c'} = (\varepsilon_c - \varepsilon_v)\delta_{vv'}\delta_{cc'} \tag{16}$$

$$K^{\text{x}}_{vc,v'c'} = \int \phi^*_c(\mathbf{r})\phi_v(\mathbf{r})v_{\text{C}}(\mathbf{r},\mathbf{r}')\phi_{c'}(\mathbf{r}')\phi^*_{v'}(\mathbf{r}')\text{d}^3\mathbf{r}\,\text{d}^3\mathbf{r}' \tag{17}$$

$$K^{\text{d}}_{vc,v'c'} = \int \phi^*_c(\mathbf{r})\phi_{c'}(\mathbf{r})\phi_v(\mathbf{r}')\phi^*_{v'}(\mathbf{r}') \tag{18}$$

$$\times W(\mathbf{r},\mathbf{r}',\omega=0)\text{d}^3\mathbf{r}\,\text{d}^3\mathbf{r}'\,. \tag{19}$$

For a spin-singlet ground state and spin-orbit coupling that is small compared to the electron-hole coupling, the BSE solutions can be classified as spin-singlet and spin-triplet excitations, respectively. Exploiting this allows one to find solutions only for the spin type of interest, e.g., for spin-singlet excitations by using

$$H^{\text{res}}_{vc,v'c'} = D_{vc,v'c'} + K^{\text{d}}_{vc,v'c'} + 2K^{\text{x}}_{vc,v'c'} \tag{20}$$

$$K_{cv,v'c'} = K^{\text{d}}_{cv,v'c'} + 2K^{\text{x}}_{cv,v'c'}. \tag{21}$$

Projection-based-embedding

Projection-based embedding (PbE) is a formally exact DFT-in-DFT embedding scheme[32], which starts from a standard DFT calculation on the whole system and its atomic orbital (AO) basis. Using a unitary transformation, the N occupied molecular orbitals from this calculation are then first transformed into localized orbitals, $\phi_i^{\text{LO}}(\mathbf{r})$. By specifying a set of atoms in the active region A, those localized orbitals with a significant Mulliken population $q_i^{\text{A}} > q_t$ on these atoms ($q_t = 0.4$ is recommended in Ref. 32) are used to construct an initial active density $n^{\text{A}}(\mathbf{r})$:

$$n^{\text{A}}(\mathbf{r}) = 2 \sum_{\substack{i=1 \\ q_i^{\text{A}} > q_t}}^{N} \left|\phi_i^{\text{LO}}(\mathbf{r})\right|^2. \tag{22}$$

With that, the density of the inactive region B is determined as $n^{\text{B}}(\mathbf{r}) = n(\mathbf{r}) - n^{\text{A}}(\mathbf{r})$. Following this initial partition of the total reference density,$n^{\text{A}}(\mathbf{r})$ is considered a variable here indicated as $\tilde{n}^{\text{A}}(\mathbf{r})$. A self-consistent calculation on the electrons in subsystem A embedded in the density of region B (A-in-B) employs the Fock matrix

$$\underline{\mathbf{F}}^{\text{A-in-B}} = \underline{\mathbf{h}}_{\text{core}}^{\text{A-in-B}}[n^{\text{A}}, n^{\text{B}}] + \underline{\mathbf{J}}[\tilde{n}^{\text{A}}] + \underline{\mathbf{K}}[\tilde{n}^{\text{A}}] + \underline{\mathbf{V}}_{\text{xc}}[\tilde{n}^{\text{A}}], \tag{23}$$

where $\underline{\mathbf{J}}$, $\underline{\mathbf{K}}$, and $\underline{\mathbf{V}}_{\text{xc}}$ are Hartree, exchange, and exchange-correlation matrices depending on the active density. In contrast, the embedded core Hamiltonian

$$\begin{aligned} \underline{\mathbf{h}}_{\text{core}}^{\text{A-in-B}}[n^{\text{A}}, n^{\text{B}}] = \underline{\mathbf{h}}_{\text{core}} &+ \underline{\mathbf{J}}[n^{\text{A}} + n^{\text{B}}] - \underline{\mathbf{J}}[n^{\text{A}}] \\ &+ \underline{\mathbf{K}}[n^{\text{A}} + n^{\text{B}}] - \underline{\mathbf{K}}[n^{\text{A}}] \\ &+ \underline{\mathbf{V}}_{\text{xc}}[n^{\text{A}} + n^{\text{B}}] - \underline{\mathbf{V}}_{\text{xc}}[n^{\text{A}}] + \mu \mathbf{P}_{\text{B}} \end{aligned} \tag{24}$$

is based on the initially partitioned densities n^{A} and n^{B} and contains the core Hamiltonian of the full system, the difference between the Hartree, exchange, and exchange-correlation terms for the full system and the initially chosen active subsystem, respectively. It also contains a projection term $\mu\underline{\mathbf{P}}_{\mathrm{B}}$ with the projection operator

$$\underline{\mathbf{P}}_{\mathrm{B}} = \underline{\mathbf{S}}\underline{\mathbf{D}}^{\mathrm{B}}\underline{\mathbf{S}} \tag{25}$$

based on the density matrix $\underline{\mathbf{D}}^{\mathrm{B}}$ of the environment and the atomic orbital overlap matrix $\underline{\mathbf{S}}$ to ensure orthogonality between the occupied states of the environment and the rest of the active subsystem. Formally, this is exactly the case in the limit $\mu \to \infty$. For practical calculations, using a value of $\mu = 10^5$ Hartree is sufficient[32].

A GW-BSE calculation can be performed on an active region using a ground state based on a PbE-DFT calculation. There are no changes in the procedure for the GW-BSE steps as outlined above, except that all quantities involved use the embedded Kohn–Sham molecular orbitals and their energies as a starting point. However, compared to a (fictional) full GW-BSE calculation, the screening in Eq. (8) lacks contributions of transitions from the 'occupied' inactive orbitals[18]. We have also shown previously that the effects of this on *relative excitation energies*, as are relevant for, e.g., Marcus rates, are small[19] for the kind of systems studied in this work.

Excitonic processes at a DPP2Py2T-PCBM interface

In Ref. 24 we have reported final structures of a DPP2Py2T-PCBM[60] blend from the simulated evaporation of chloroform solvent. Of these large-scale structures, we first select the DPP2Py2T and PCBM[60] with the closest center of mass distance from each fragment to C_{60} center-of-mass as they are expected to exhibit the strongest interactions between the donor and acceptor molecule and potentially the energetically lowest lying CT excitation energies. As this dimer structure still contains in total 650 atoms, we remove in a first post-processing step the side chains of DPP2Py2T (excluding one methyl group) and replace PCBM[60] with a plain C_{60} at the same position and orientation. This step reduces the number of atoms to 262, and the corresponding structure is shown in Figure 1.

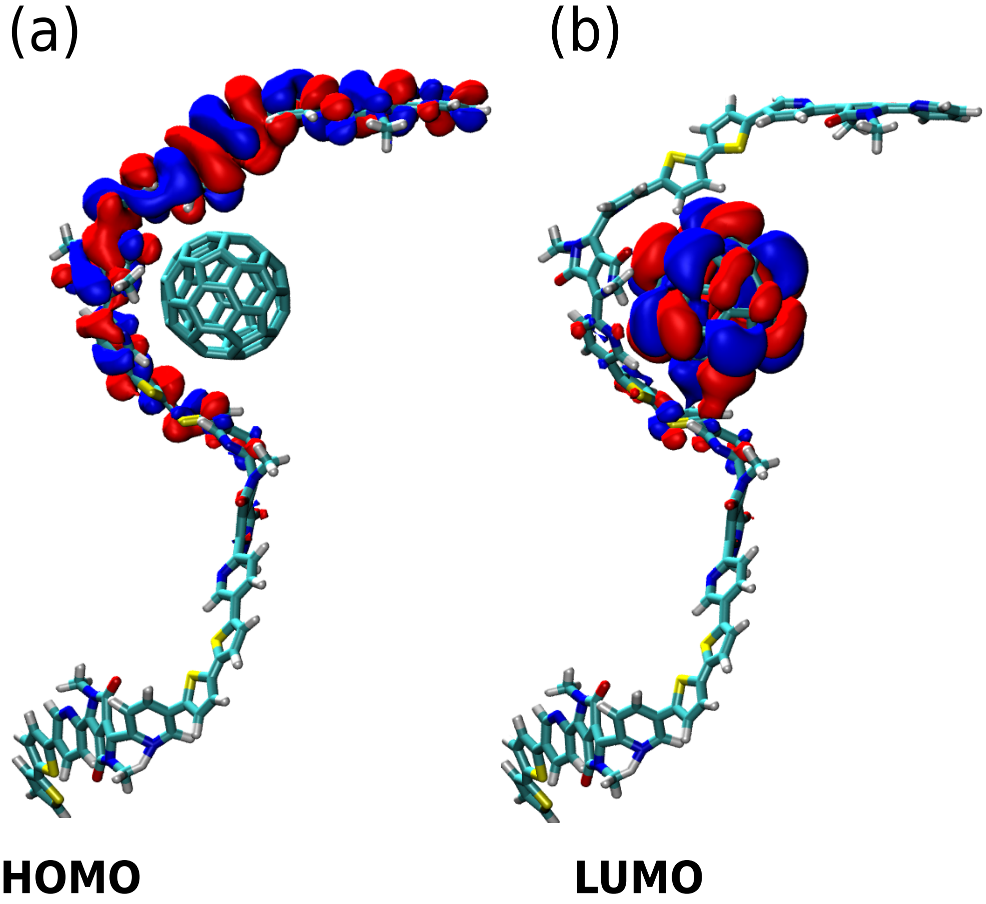

Figure 1: Isosurfaces of the full KS HOMO and LUMO (isovalues ±0.005 a_B^{-3}) for the DPP2Py2T-PCBM[60] structures taken from the final results of solvent evaporation approaches from Ref.[24] after removing side chains.

To keep subsequent calculations on the electronic structure tractable, we then use Stuttgart-Dresden effective core potentials[33] with an uncontracted version of the associated optimized basis set, augmented by polarization functions from the 6-311G** basis[34]. It was shown in[35] that this basis set offers a good balance between the computational cost of GW-BSE calculations and the absolute precision. In all calculations, the hybrid functional PBE0[36] has been used in steps that involve KS-DFT.

With these choices, the number of electrons in the full system is 898, so 449 occupied levels, with a total basis set size of 4692. Therefore, a full GW-BSE calculation would have in the most extreme case $N_{\mathrm{RPA}} = 1905107$ transitions in the screening calculations, with the

BSE product space $N_{\mathrm{BSE}} = 996004$, and the computational cost is enormous.

Inspecting the orbital distributions of HOMO and LUMO for the selected structure in Figure 1 obtained from full KS-DFT calculations reveals that the HOMO is not delocalized throughout the DPP2Py2T chain but remains localized on the part close to the C_{60} molecule. It should be noted that the LUMO extends slightly from the fullerene to the polymer chain. Based on these observations, we proceed with a PbE setup, in which the active region comprises the end 2-mer of DPP2Py2T and the C_{60}, in total 262 atoms.

Interface Excitons

In this chosen setting, there are 644 active electrons, so 322 occupied states in the PbE-GW-BSE calculation, and the number of transitions in the RPA is 140714. We calculate quasiparticle energies in one shot G_0W_0 for the lowest 964 states, using a generalized plasmon-pole model for the frequency dependence of the dielectric function[37,38]. The electron-hole wave function is expanded into product states of 322 occupied with 644 virtual states, leading to a total dimension of the product space of 207368. The BSE is then solved for the 30 lowest-energy singlet excitations.

First, we notice a variety of different characters in the calculated excitations, not only between localized excitations (LE) and charge-transfer (CT) excitations but also especially regarding the finer details of the latter. In Figure 2(a) we show the five typical classes of excitations we can identify with isosurfaces of electron difference densities (blue: electron density; red: hole density): localized excitations on the polymer (LE_{P}), localized excitations on the fullerene (LE_{F}), integer CT excitations with hole on the thiophenes of DPP2Py2T ($\mathrm{CT}_{\mathrm{int}}^{\mathrm{hT}}$), integer CT excitations with hole on the DPP unit ($\mathrm{CT}_{\mathrm{int}}^{\mathrm{hD}}$), and partial CT excitations ($\mathrm{CT}_{\mathrm{part}}$). For each of these types, there are, in general, multiple excitations, as can be seen from the energy level diagram in Figure 2(b), where we marked the energy levels according to their dominant character. The energy spectrum is relatively dense as all 30 excitations are found in an energy range from 1.5 eV to 2.4 eV. Focusing first on the lowest energies, as they

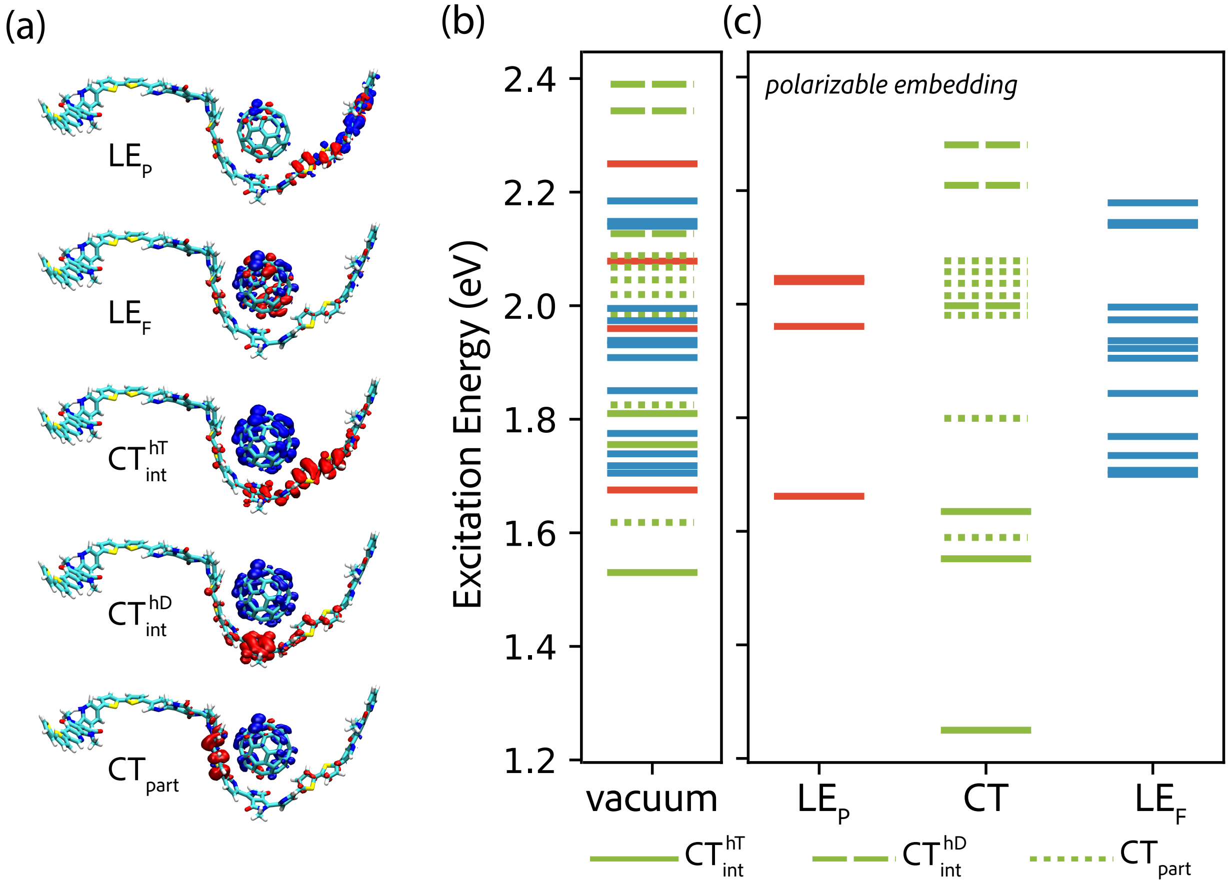

Figure 2: Excitons at the DPP2Py2T-PCBM[60] interface as resulting from PbE-G_0W_0-BSE calculations. (a) Isosurfaces ($\pm 0.0008\,\mathrm{e a_B^{-3}}$) of the electron difference densities for five typical types of excitations: localized excitations on the polymer (LE$_\mathrm{P}$), localized excitations on the fullerene (LE$_\mathrm{F}$), integer CT excitations with hole on the thiophenes of DPP2Py2T (CT$^\mathrm{hT}_\mathrm{int}$), integer CT excitations with hole on the DPP unit (CT$^\mathrm{hD}_\mathrm{int}$), and partial CT excitations (CT$_\mathrm{part}$). (b) Energy levels of the lowest 30 singlet excitation energies (in eV) in vacuum. Solid red lines indicate LE$_\mathrm{P}$, solid blue lines LE$_\mathrm{F}$, green lines different CT type excitation (solid: CT$^\mathrm{hT}_\mathrm{int}$, dashed: CT$^\mathrm{hD}_\mathrm{int}$, dotted: CT$_\mathrm{part}$), respectively. (c) Final interface excitation energy levels after polarizable lattice embedding, split for LE and CT type of excitations.

are more relevant for the excitonic conversion processes, we find that the lowest excitation with $\Omega = 1.53\,\mathrm{eV}$ is an integer CT excitation with the hole density found on the electron-donating moieties of the DPP2Py2T polymer. Interestingly, the second-lowest excitation ($1.61\,\mathrm{eV}$) is a partial CT excitation (with a charge transfer of $0.4\,\mathrm{e}$). At $\Omega = 1.68\,\mathrm{eV}$ and $\Omega = 1.71\,\mathrm{eV}$ we find the two lowest LE in the polymer and C_{60}, respectively. The second lowest excitation of $\mathrm{CT}^{\mathrm{hT}}_{\mathrm{int}}$ type is obtained at $1.76\,\mathrm{eV}$, above both LE excitations. We note that the integer CT excitations with the hole localized on a DPP unit of DPP2Py2T are at much higher energy above $2.1\,\mathrm{eV}$. From experiment[10], the optical gaps of DPP2Py2T and PCBM[60] are reported as $1.70\,\mathrm{eV}$ and $1.75\,\mathrm{eV}$, respectively, and our PbE-G_0W_0-BSE results are in good agreement with them. Ref. 10 does not state energies of the CT states explicitly, but the indication from their spectroscopy data seems to suggest an energy offset between the lowest CT excitation and the two LE of about $> 0.4\,\mathrm{eV}$ and the existence of a relevant second CT state roughly $0.3\,\mathrm{eV}$ higher than the first one. We assume that the spectroscopically relevant CT states are the $\mathrm{CT}^{\mathrm{hT}}_{\mathrm{int}}$ type excitation and not the one with partial charge transfer as they would not lead to charge separation, and for brevity we refer to the two lowest excitations of that type as CT_1 and CT_2, respectively. Our calculations yield a too small offset for CT_1 and an energy for CT_2 that is, most importantly, above those of the two LE, very much in contrast to the experimental evidence.

Polarizable embedding

However, it is known from previous studies[16,35,39] that charge transfer excitations are especially sensitive to polarizable molecular environments. To account for such effects, we follow the idea of Ref.[39] and embed the quantum-quantum embed PbE-G_0W_0-BSE embedded calculation on the DPP2Py2T-PCBM[60] complex in a polarizable lattice model. First, a regular $n \times n \times n$ grid is created centered around the complex, with lattice spacing a. Then, all lattice points within the van-der-Waals surface of the complex are removed. Each lattice point m is assigned an isotropic dipole polarizability α_m, which allows the formation of induced dipoles $\boldsymbol{\mu}_m = \alpha_m \mathbf{F}_m$ as the response to the total electric field at the lattice site, $\mathbf{F}_m$, with contributions from the induced dipoles at the other lattice sites and from the field of the explicit electronic density of the complex. The total lattice energy of this model is then

$$E_{\text{lat}}^{(s)} = \sum_m \sum_{m' \neq m} \boldsymbol{\mu}^{m(s)} (\alpha^{-1})^{mm'} \boldsymbol{\mu}^{m'(s)}, \tag{26}$$

where the index s is used to differentiate between the different responses to different states of the PbE-G_0W_0-BSE calculation. This energy follows a variational principle with respect to the induced moments. A preconditioned conjugate gradient method is used to find the $\boldsymbol{\mu}^{m(s)}$, which give the minimum energy. Induced interactions are modified using Thole's damping functions[40,41] to avoid overpolarization. For the calculation of the electronic density in the PbE-G_0W0-BSE region and the calculation of its electric field, we determine

$$n^{(s)}(\mathbf{r}) = \tilde{n}^{\text{A}}(\mathbf{r}) + n^{\text{B}}(\mathbf{r}) + n_e^{(s)}(\mathbf{r}) - n_h^{(s)}(\mathbf{r}). \tag{27}$$

Here, the electron (hole) contribution of the exciton to the density is computed by integrating the squared excited-state wavefunction ζ_S with respect to the hole (electron) coordinates, i.e.

$$\begin{aligned} n_{\text{e}}^{(s)}(\mathbf{r}) = n_{\text{e}}^{(s)}(\mathbf{r}_{\text{e}}) &= \int d\mathbf{r}_{\text{h}} |\zeta_S(\mathbf{r}_{\text{e}}, \mathbf{r}_{\text{h}})|^2 \\ n_{\text{h}}^{(s)}(\mathbf{r}) = n_{\text{h}}^{(s)}(\mathbf{r}_{\text{h}}) &= \int d\mathbf{r}_{\text{e}} |\zeta_S(\mathbf{r}_{\text{e}}, \mathbf{r}_{\text{h}})|^2. \end{aligned} \tag{28}$$

$$E_{\text{QM}}^{(s)} = E_{\text{DFT}}^{(s)} + \delta_{sx}\, \Omega_S. \tag{29}$$

The associated total electron density is then evaluated on a grid. The minimized lattice energy $E_{\text{lat}}^{(s)}$ is used to update the total energy of the coupled QM/MM system

$$E_{\text{QM/MM}}^{(s)} = E_{\text{QM}}^{(s)} + E_{\text{lat}}^{(s)}. \tag{30}$$

To obtain the excitation energy $\Omega^{(s)}$ of a complex in the polarizable environment, total energies of the combined QM/MM system are obtained for both the ground and the excited state, and their difference defines

$$\Omega^{(s)} = E_{\text{QM/MM}}^{(s)} - E_{\text{QM/MM}}^{(n)}. \tag{31}$$

The resulting quantum-quantum-classical (PbE-G_0W_0-BSE/lattice) embedded excitation energies for the localized and charge-transfer excitations are shown in Fig. 2(c). Because the localized excitations show only relatively small changes in the total dipole moments of the complex, the lattice embedding effect on their excitation energies is small, especially for the lowest LE excitations. In contrast, CT states show a significant reduction in their excitation energy, most notably resulting in CT_1 being found 0.28 eV lower in energy and CT_2 0.20 eV lower, respectively, both now below the energy of the two LEs in polymer and fullerene. With the environment effects, this now holds even for the next $\text{CT}_{\text{int}}^{\text{hT}}$ excitation (CT_3).

It is tempting to infer from these alignments of the excitation energy levels something regarding the respective driving forces of dynamical processes, such as the conversion from the LE to CT states. However, vertical excitation energies such as those in Fig. 2 alone do not provide an exhaustive description of such processes.

Reorganization energy estimates and adiabatic energies

Although these calculations will provide crucial information on the different vertical excitation energies, the evaluation of the Marcus rates Eq. (1) further requires the determination of the respective reorganization energies $\lambda_{\text{LE-CT}}$ and in general the adiabatic excitation energies instead of the vertical ones. Within the Marcus picture, $\lambda_{\mathrm{LE_x-CT}} = E_{\mathrm{CT}}(\mathrm{LE_x}) - E_{\mathrm{CT}}(\mathrm{CT})$, where $x = \mathrm{P,F}$ (P: polymer, F: fullerene) and $E_a(G)$ represent the total energy of state a in the geometry of state G. As such, this would require the cumbersome optimization of the dimer structures in the respective CT and LE states within PbE-G_0W_0-BSE. Instead, we approximate the energies from monomer calculations in vacuum, such that

$$E_{\mathrm{CT}}(\mathrm{LE_P}) = E_{\mathrm{P}}^{+}(\mathrm{P}^{*}) + E_{\mathrm{F}}^{-}(\mathrm{F}^{0}) \tag{32}$$

$$E_{\mathrm{CT}}(\mathrm{LE_F}) = E_{\mathrm{P}}^{+}(\mathrm{P}^{0}) + E_{\mathrm{F}}^{-}(\mathrm{F}^{*}) \tag{33}$$

$$E_{\mathrm{CT}}(\mathrm{CT}) = E_{\mathrm{P}}^{+}(\mathrm{P}^{+}) + E_{\mathrm{F}}^{-}(\mathrm{F}^{-}) \tag{34}$$

where the superscripts refer to the state of the monomers (0: ground state, +: cation, −: anion, ∗: excited). The total energy calculations and geometry optimizations in this step are performed using (time-dependent) DFT with the def2-tzvp basis set and PBE0 functional. For DPP2Py2T we perform these calculations on two repeat units because the hole part of the excited states remains localized on such a smaller subpart of the full structure as in Figure 1. With this, we obtain $\lambda_{\mathrm{LE_P\text{-}CT}} = 0.10\,\mathrm{eV}$, $\lambda_{\mathrm{LE_F\text{-}CT}} = 0.24\,\mathrm{eV}$, $\lambda_{\mathrm{CT\text{-}LE_P}} = 0.14\,\mathrm{eV}$, and $\lambda_{\mathrm{CT\text{-}LE_F}} = 0.21\,\mathrm{eV}$, respectively. In similar spirit, we determine the vertical to adiabatic energy relaxations of the excited states, $\Lambda_a = E_a(0) - E_a(A)$, and find $\Lambda_{\mathrm{LE_P}} = \Lambda_{\mathrm{LE_F}} = 0.18\,\mathrm{eV}$ and $\Lambda_{\mathrm{CT}} = 0.19\,\mathrm{eV}$, respectively. As a consequence, adiabatic corrections to the vertical excitation energy differences discussed above hardly influence the driving forces $\Delta E_{\mathrm{LE\text{-}CT}}$ in Eq. (1).

Non-adiabatic LE-CT couplings

The other required quantities are the non-adiabatic coupling elements between LE and CT excitons. As the excitations considered so far are solutions of the BSE and therefore adiabatic states $|\Phi_i\rangle$ of some electronic Hamiltonian $\mathrm{H_{el}}$, corresponding diabatic states can be obtained via a unitary transformation. We employ specifically two-state diabatization within the

Fragment Charge Difference approach, in which the diabatic states are eigenstates of the so-called fragment charge difference (FCD) matrix[42] based on the definition of donor (D) and acceptor (A) fragments, as $\Delta Q_{ij} = Q_{ij}(D) - Q_{ij}(A)$. Fragment charges are typically obtained from a population analysis of the individual adiabatic densities and the transition density between them[43]. For a two-state model, the coupling is given explicitly by

$$J_{12}^{\mathrm{FCD}} = \frac{|\Delta Q_{12}|(\Omega_2 - \Omega_1)}{((\Delta Q_{11} - \Delta Q_{22})^2 + 4\Delta Q_{12}^2)^{1/2}}. \tag{35}$$

Due to the near-degeneracy of the three lowest fullerene excitations, we consider the coupling elements between each of these with the three lowest CT excitations. For the polymer, a single LE is used. The resulting squared coupling elements for the DPP2Py2T-PCBM[60] system are given in Table 1. For all twelve transitions, the values range from $1.1 \cdot 10^{-3}\,(\mathrm{eV})^2$ (for the coupling between the lowest LE in fullerene and the lowest CT excitation) to $1.3 \cdot 10^{-6}\,(\mathrm{eV})^2$ (for the coupling between the lowest LE on fullerene and the second lowest CT excitation). In particular, for the coupling between the lowest LE on the polymer with the CT states, and the respective one of the lowest LE on fullerene, we find a difference of less than one order of magnitude. Overall, the differences among the squared coupling elements alone do not seem to indicate a clear underlying reason for the experimentally observed differences in charge generation.

Rates and Activation Energies

Bringing excitation energies, reorganization energies, and coupling elements together then produces quantitative predictions for the LE to CT transition rates (evaluated at room temperature) as given in Table 1. It can be seen that most of the rates are in the range $> 10^{12}\,\mathrm{s}^{-1}$, with the notable exception of the rate for the $\mathrm{LE_P}$-$\mathrm{CT_1}$ ($1.1 \cdot 10^9\,\mathrm{s}^{-1}$) and $\mathrm{LE_{F_1}}$-$\mathrm{CT_2}$ ($3.2 \cdot 10^{10}\,\mathrm{s}^{-1}$) transitions, respectively. The latter can be traced back to the low value of the associated coupling element. For the former, the situation is less clear, as the coupling

Table 1: Transition specific parameters for the LE to CT transitions at the DPP2Py2T-PCBM[60] interface.

	ΔE/eV	$J^2/(\mathrm{eV})^2$	ω/s^{-1}	E_{act}/eV
$\mathrm{LE_P}$-$\mathrm{CT_1}$	0.41	$3.9 \cdot 10^{-4}$	$1.1 \cdot 10^{9}$	0.25
$\mathrm{LE_P}$-$\mathrm{CT_2}$	0.11	$5.7 \cdot 10^{-5}$	$3.0 \cdot 10^{12}$	0.00
$\mathrm{LE_P}$-$\mathrm{CT_3}$	0.03	$4.2 \cdot 10^{-5}$	$1.4 \cdot 10^{12}$	0.01
$\mathrm{LE_{F_1}}$-$\mathrm{CT_1}$	0.45	$1.1 \cdot 10^{-3}$	$6.1 \cdot 10^{12}$	0.05
$\mathrm{LE_{F_1}}$-$\mathrm{CT_2}$	0.15	$1.3 \cdot 10^{-6}$	$3.2 \cdot 10^{10}$	0.01
$\mathrm{LE_{F_1}}$-$\mathrm{CT_3}$	0.07	$5.5 \cdot 10^{-5}$	$5.8 \cdot 10^{11}$	0.03
$\mathrm{LE_{F_2}}$-$\mathrm{CT_1}$	0.46	$6.4 \cdot 10^{-4}$	$3.0 \cdot 10^{12}$	0.05
$\mathrm{LE_{F_2}}$-$\mathrm{CT_2}$	0.16	$3.4 \cdot 10^{-4}$	$9.1 \cdot 10^{12}$	0.01
$\mathrm{LE_{F_2}}$-$\mathrm{CT_3}$	0.07	$2.2 \cdot 10^{-5}$	$2.5 \cdot 10^{11}$	0.03
$\mathrm{LE_{F_3}}$-$\mathrm{CT_1}$	0.49	$1.2 \cdot 10^{-3}$	$3.4 \cdot 10^{12}$	0.07
$\mathrm{LE_{F_3}}$-$\mathrm{CT_2}$	0.18	$2.2 \cdot 10^{-3}$	$6.7 \cdot 10^{13}$	0.01
$\mathrm{LE_{F_3}}$-$\mathrm{CT_3}$	0.10	$1.6 \cdot 10^{-4}$	$2.6 \cdot 10^{12}$	0.02

element is not significantly smaller and the driving force ΔE is large. To scrutinize the origin of this low rate, we consider in addition the activation energy within with Marcus picture

$$E_{\mathrm{act}} = (\Delta E - \lambda)^2/(4\lambda) \tag{36}$$

and also list the results in Table 1. While most of the transitions show small activation energies of 0.05 eV or less, the $\mathrm{LE_P}$-$\mathrm{CT_1}$ is a notable exception showing an activation energy of 0.25 eV. Such a high activation energy is likely the reason for the observed small rate for transitions from the lowest polymer excitation to the lowest CT excitation.

Dynamical Model

To gain insight into conversion dynamics, we employ a kinetic model that describes the time evolution of the probabilities of the state population $\mathbf{P}(t)$ via a system of ordinary differential equations of the kind

$$\frac{d}{dt}\mathbf{P}(t) = \underline{\mathbf{W}}\mathbf{P}(t), \tag{37}$$

where $\mathbf{P}^T(t) = [P_{\mathrm{LE_P}}(t), \mathbf{P}^T_{\mathrm{LE_F}}(t), \mathbf{P}^T_{\mathrm{CT}}(t)]$ and $\sum_i P_i(t) = 1$ for all t. The entries on the off-diagonals of the matrix $\underline{\mathbf{W}}$ correspond to the respective Marcus rates for LE to CT and CT to LE transitions, respectively, as we do not consider direct transitions between different LE or different CTs. The diagonals of $\underline{\mathbf{W}}$ contain the negative of the sum of all other column entries, i.e., $W_{ii} = -\sum_j W_{ji}$.

We consider two different scenarios: a 5-state model in which we only take the lowest LE on the fullerene into account, and a 7-state model in which we take the three lowest into account due to their near-degeneracy. For each of these scenarios, we prepare the initial populations to mimic the initial excitations of LEs on polymer and fullerene, respectively, i.e., by setting $\mathbf{P}^T_{\mathrm{P}}(t=0) = [1, 0, \ldots, 0]$ for polymer excitation,$\mathbf{P}^T_{\mathrm{F}}(t=0) = [0, 1, 0, \ldots, 0]$ for fullerene excitation in the model with a single fullerene level, and $\mathbf{P}^T_{\mathrm{F}}(t = 0) = [0, 0.47, 0.36, 0.13, 0, 0, 0]$ (Boltzmann populations) in the model with three fullerene LEs. For each of these initial populations, we numerically study the evolution of Eq. (37) for $t_{\max} = 1\,\mathrm{ns}$ using the backward Euler scheme[44] with 10^5 steps. We note that (i) as we can only model the LE-to-CT transitions (and vice versa) and not the subsequent processes of excitation transferring away from the interface and (ii) we only consider a fixed molecular geometry, we limit ourselves to the ns timescale in total and expect the relevant fast initial decay processes from LE to CT states to occur on the timescales of several ps. Within this model, by construction in the long-time limit, the system will fully populate CT_1 as equilibrium state. Hence, the focus lies on the short-time behavior of the population dynamics.

Figure 3 shows the time-dependent state probabilities obtained for the 5-state (top row) and 7-state model (bottom row), respectively, for the two initial excitation scenarios. Considering first the dynamics in the 5-state model after polymer excitation in Figure 3(a) we observe that the polymer LE depopulates within one ps. Initially, CT_2 and to a lesser extent CT_3 become populated. On the ps timescale, there is hardly any population of the lowest CT state. At longer times, the two higher energy CT states begin to depopulate towards

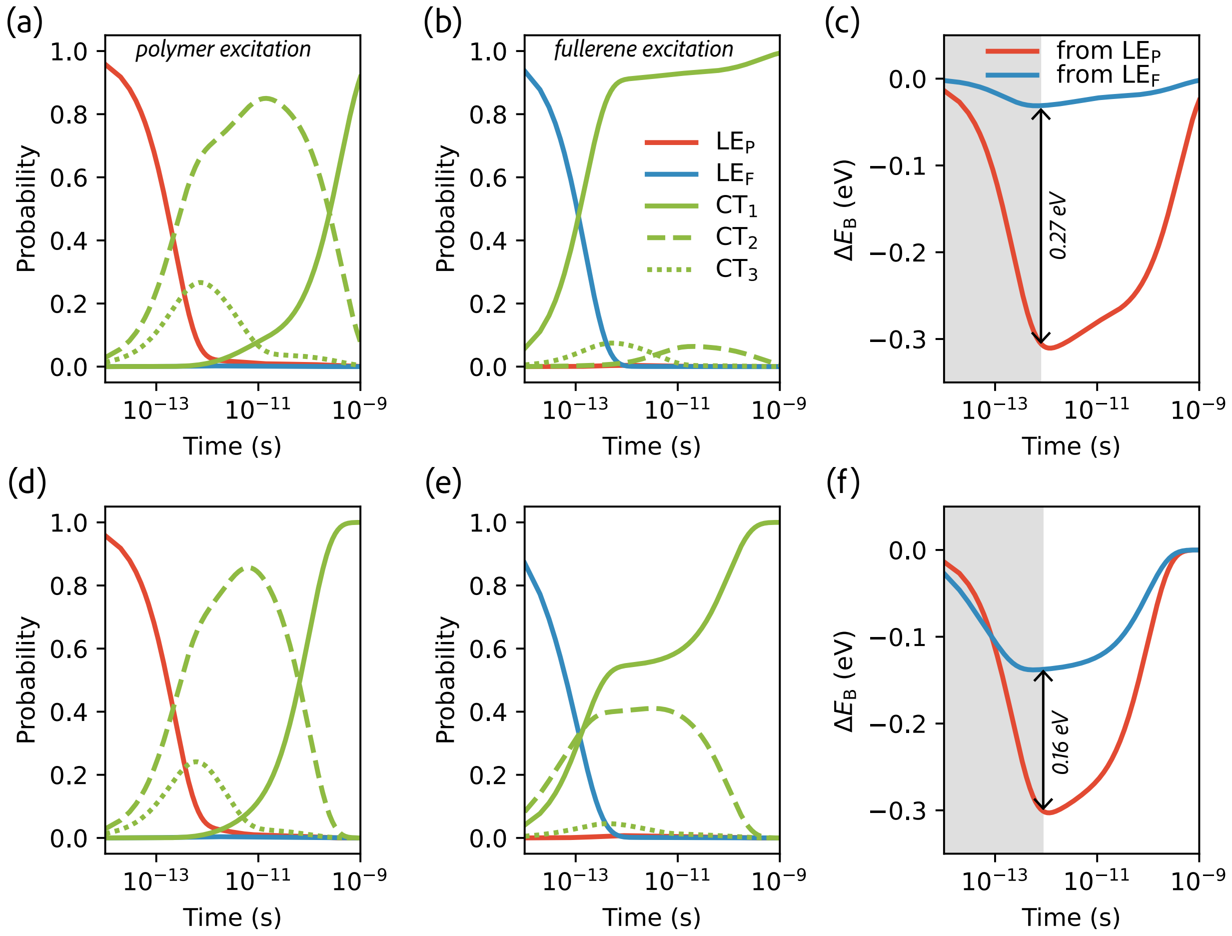

Figure 3: Results of the state dynamics in the 5-state-model (top row) and 7-state model (bottom row), respectively: Time-dependent state probabilities (a,d) after excitation of the polymer; after excitation of the fullerene (b,e). Expected exciton binding energy difference ΔE_B to the binding energy of pure CT_1 (c,f).

CT_1, approaching the equilibrium state at 1 ns. In contrast, while the dynamical behavior after fullerene excitation exhibits a similar decay of the respective LE, it is almost exclusively CT_1 that becomes populated within the first ps. To scrutinize how these two different dynamics translate into the experimentally observed different charge generation, we consider the *effective exciton binding energies* in the CT states. For each state, the binding energy is the difference between the CT excitation energy and the energy E_CS or the charge separated state, that is, $E_\mathrm{B}^i = E_\mathrm{CS} - \Omega_{\mathrm{CT}_i}$. As E_CS is not easily calculable, we instead consider the reduction in the effective exciton binding energy compared to the binding energy of CT_1 in the time-dependent expectation value of the CT energy as

$$\Delta E_{\mathrm{B}}(t) = \sum_{i=1}^{3} P_{\mathrm{CT}_i}(t)\Omega_{\mathrm{CT}_i} - \Omega_{\mathrm{CT}_1}. \tag{38}$$

We present in Figure 3(c) the relative binding energy reduction over time for the excitation of polymer (red) and fullerene (blue), respectively. The gray shaded area indicates the fast picosecond timescale we consider relevant for the initial decay of the LE to CT states and subsequent generation of free charges. It is clearly visible that due to the different population dynamics the effective CT binding energy is 0.27 eV lower after polymer excitation compared to fullerene excitation. In other words, relative to an initial excitation of the polymer, an additional driving force of nearly 0.3 eV is needed to separate the electron-hole pair after fullerene excitation. Ultimately, from our embedded PbE-G_0W_0-BSE calculations, we can trace the dichotomous nature of exciton conversion at the DPP2Py2T-PCBM interface back to the difference in which CT state becomes populated depending on the initial LE formation, which again is a consequence of the large activation energy needed to populate the more strongly bound CT_1 state from the polymer.

Finally, we briefly comment on the results obtained from the 7-state model, showing the time-dependent populations and effective binding energy reduction in Figure 3(d)-(f). The main difference to the 5-state model concerns the populations after fullerene excitation in panel (e). Here, one can see that on the relevant timescale of ps, the populations of CT_1 and CT_2 evolve roughly similarly. From the contribution of the population of the less strongly bound CT_2, the effective binding energy reduction as defined by Eq. (38) after fullerene excitation is stronger compared to the result in the 5-state model. As a consequence, the additional driving force for charge separation compared to polymer excitation is reduced by about 0.1 eV. Importantly, the details of the underlying processes and the conclusions regarding the origin of the dichotomous exciton conversion at the DPP2Py2T-PCBM interface are the same in both models.

Summary

We employed projection-based embedded GW-Bethe–Salpeter equation (PbE-GW-BSE) calculations to elucidate the microscopic origins of dichotomous exciton conversion at a DPP2Py2T-PCBM interface. Our analysis reveals that depending on whether the donor or acceptor is initially photoexcited, distinct charge-transfer (CT) states are preferentially populated. Specifically, donor excitation leads predominantly to higher-lying, less tightly bound CT states, while acceptor excitation facilitates direct population of the lowest-energy CT state. This behavior arises from a markedly larger activation energy barrier for exciton conversion from the polymer to the most strongly bound CT state. Kinetic modeling confirms that these differences manifest on sub-nanosecond timescales, resulting in a lower effective exciton binding energy following donor excitation. These findings provide a mechanistic understanding of the experimentally observed dichotomous charge generation in organic solar cells and underscore the importance of initial excitation conditions in determining device performance. Crucially, these insights were made possible by recent technical advances in quantum-quantum-classical embedding, which enable many-body Green's function calculations on interfacial systems of realistic molecular complexity.

Acknowledgement

We acknowledge support by the Innovational Research Incentives Scheme Vidi of the Netherlands Organisation for Scientific Research (NWO) with project number 723.016.002. Partial funding is also provided by NWO and the Netherlands eScience Center for funding through project number 027.017.G15, within the Joint CSER and eScience program for Energy Research (JCER 2017). We thank Alexey V. Lyulin for the critical reading of the manuscript. All PbE-G_0W_0-BSE calculations were performed on the `Snellius` supercomputer of the Dutch national e-infrastructure. with the support of the SURF Cooperative using grant no. EINF-4183.

References

(1) Brabec, C. J.; Sariciftci, N. S.; Hummelen, J. C. Plastic Solar Cells. *Adv. Funct. Mater.* **2001**, *11*, 15–26.

(2) Deibel, C.; Dyakonov, V. Polymer-Fullerene Bulk Heterojunction Solar Cells. *Rep. Prog. Phys.* **2010**, *73*, 096401.

(3) Li, W.; Hendriks, K. H.; Wienk, M. M.; Janssen, R. A. Diketopyrrolopyrrole Polymers for Organic Solar Cells. *Acc. Chem. Res.* **2016**, *49*, 78–85.

(4) Wienk, M. M.; Turbiez, M.; Gilot, J.; Janssen, R. A. Narrow-bandgap diketo-pyrrolo-pyrrole polymer solar cells: The effect of processing on the performance. *Adv. Mater.* **2008**, *20*, 2556–2560.

(5) Chandran, D.; Lee, K.-S. Diketopyrrolopyrrole: A Versatile Building Block for Organic Photovoltaic Materials. *Macromol. Res.* **2013**, *21*, 272–283.

(6) Choi, H.; Ko, S. J.; Kim, T.; Morin, P. O.; Walker, B.; Lee, B. H.; Leclerc, M.; Kim, J. Y.; Heeger, A. J. Small-bandgap polymer solar cells with unprecedented short-circuit current density and high fill factor. *Adv. Mater.* **2015**, *27*, 3318–3324.

(7) Ashraf, R. S.; Meager, I.; Nikolka, M.; Kirkus, M.; Planells, M.; Schroeder, B. C.; Holliday, S.; Hurhangee, M.; Nielsen, C. B.; Sirringhaus, H. et al. Chalcogenophene comonomer comparison in small band gap diketopyrrolopyrrole-based conjugated polymers for high-performing field-effect transistors and organic solar cells. *J. Am. Chem. Soc.* **2015**, *137*, 1314–1321.

(8) Hendriks, K. H.; Heintges, G. H.; Gevaerts, V. S.; Wienk, M. M.; Janssen, R. A. High-molecular-weight regular alternating diketopyrrolopyrrole-based terpolymers for efficient organic solar cells. *Angew. Chem. Int. Ed.* **2013**, *52*, 8341–8344.

(9) Heinrichová, P.; Pospíšil, J.; Stříteský, S.; Vala, M.; Weiter, M.; Toman, P.; Rais, D.; Pfleger, J.; Vondráček, M.; Šimek, D. et al. Diketopyrrolopyrrole-Based Organic Solar Cells Functionality: The Role of Orbital Energy and Crystallinity. *J. Phys. Chem. C* **2019**, *123*, 11447–11463.

(10) Hendriks, K. H.; Wijpkema, A. S. G.; van Franeker, J. J.; Wienk, M. M.; Janssen, R. A. J. Dichotomous Role of Exciting the Donor or the Acceptor on Charge Generation in Organic Solar Cells. *J. Am. Chem. Soc.* **2016**, *138*, 10026–10031.

(11) Marcus, R. A. On the Theory of Oxidation–Reduction Reactions Involving Electron Transfer. I. *J. Chem. Phys.* **1956**, *24*, 966–978.

(12) Marcus, R. A. Electron Transfer Reactions in Chemistry. Theory and Experiment. *Rev. Mod. Phys.* **1993**, *65*, 599–610.

(13) Gélinas, S.; Rao, A.; Kumar, A.; Smith, S. L.; Chin, A. W.; Clark, J.; van der Poll, T. S.; Bazan, G. C.; Friend, R. H. Ultrafast Long-Range Charge Separation in Organic Semiconductor Photovoltaic Diodes. *Science* **2014**, *343*, 512–516.

(14) Neugebauer, J.; Jacob, C. R.; Wesolowski, T. A.; Baerends, E. J. Theoretical Spectroscopy of Embedded Molecules with the Frozen-Density Embedding Formalism. *J. Phys. Chem. A* **2005**, *109*, 7805–7814.

(15) Pavanello, M. On the subsystem formulation of linear-response time-dependent DFT. *J. Chem. Phys.* **2013**, *138*, 204118.

(16) Li, J.; D'Avino, G.; Duchemin, I.; Beljonne, D.; Blase, X. Accurate Description of Charged Excitations in Molecular Solids from Embedded Many-Body Perturbation Theory. *Phys. Rev. B* **2018**, *97*, 035108.

(17) Baumeier, B.; Andrienko, D.; Rohlfing, M. Frenkel and Charge-Transfer Excitations

in Donor–Acceptor Complexes from Many-Body Green's Functions Theory. *J. Chem. Theory Comput.* **2012**, *8*, 2790–2795.

(18) Tölle, J.; Deilmann, T.; Rohlfing, M.; Neugebauer, J. Subsystem-Based GW/Bethe–Salpeter Equation. *J. Chem. Theory Comput.* **2021**, *17*, 2186–2199.

(19) Sundaram, V.; Baumeier, B. Quantum–Quantum and Quantum–Quantum-Classical Schemes for Near-Gap Excitations with Projection-Based-Embedded GW-Bethe–Salpeter Equation. *J. Chem. Theory Comput.* **2024**, *20*, 5451–5465.

(20) Wilhelm, J.; Del Ben, M.; Hutter, J. GW in the Gaussian and Plane Waves Scheme with Application to Linear Acenes. *J. Chem. Theory Comput.* **2018**, *14*, 2348–2358.

(21) Duchemin, I.; Jacquemin, D.; Blase, X. Combining the GW Formalism with the Polarizable Continuum Model: A State-Specific Non-Equilibrium Approach. *J. Chem. Phys.* **2016**, *144*, 164106.

(22) Duchemin, I.; Guido, C. A.; Jacquemin, D.; Blase, X. The Bethe–Salpeter Formalism with Polarisable Continuum Embedding: Reconciling Linear-Response and State-Specific Features. *Chem. Sci.* **2018**, *9*, 4430–4443.

(23) Tirimbó, G.; Sundaram, V.; Baumeier, B. Embedded Many-Body Green's Function Methods for Electronic Excitations in Complex Molecular Systems. *WIREs Comput. Mol. Sci.* **2024**, *14*, e1734, e1734 CMS-1099.R1.

(24) Sundaram, V.; Lyulin, A. V.; Baumeier, B. Effect of Solvent Removal Rate and Annealing on the Interface Properties in a Blend of a Diketopyrrolopyrrole-Based Polymer with Fullerene. *J. Phys. Chem. B* **2022**, *126*, 7445–7453.

(25) Rühle, V.; Lukyanov, A.; May, F.; Schrader, M.; Vehoff, T.; Kirkpatrick, J.; Baumeier, B.; Andrienko, D. Microscopic Simulations of Charge Transport in Disordered Organic Semiconductors. *J. Chem. Theory Comput.* **2011**, *7*, 3335–3345.

(26) de Vries, X.; Friederich, P.; Wenzel, W.; Coehoorn, R.; Bobbert, P. A. Full Quantum Treatment of Charge Dynamics in Amorphous Molecular Semiconductors. *Phys. Rev. B* **2018**, *97*, 075203.

(27) Degitz, C.; Schmid, M.; May, F.; Pfister, J.; Auch, A.; Brütting, W.; Wenzel, W. From Molecule to Device: Prediction and Validation of the Optical Orientation of Iridium Phosphors in Organic Light-Emitting Diodes. *Chem. Mater.* **2023**, *35*, 295–303.

(28) Hutchison, G. R.; Ratner, M. A.; Marks, T. J. Hopping Transport in Conductive Heterocyclic Oligomers: Reorganization Energies and Substituent Effects. *J. Am. Chem. Soc.* **2005**, *127*, 2339–2350.

(29) Kohn, W.; Sham, L. J. Self-Consistent Equations Including Exchange and Correlation Effects. *Phys. Rev.* **1965**, *140*, A1133–A1138.

(30) Hedin, L. New Method for Calculating the One-Particle Green's Function with Application to the Electron-Gas Problem. *Phys. Rev.* **1965**, *139*, A796–A823.

(31) Hedin, L.; Lundqvist, S. In *Solid State Physics*; Seitz, F., Turnbull, D., Ehrenreich, H., Eds.; Academic Press, 1970; Vol. 23; pp 1–181.

(32) Manby, F. R.; Stella, M.; Goodpaster, J. D.; Miller, T. F. I. A Simple, Exact Density-Functional-Theory Embedding Scheme. *J. Chem. Theory Comput.* **2012**, *8*, 2564–2568.

(33) Bergner, A.; Dolg, M.; Küchle, W.; Stoll, H.; Preuß, H. *Ab Initio* Energy-Adjusted Pseudopotentials for Elements of Groups 13–17. *Mol. Phys.* **1993**, *80*, 1431–1441.

(34) Krishnan, R.; Binkley, J. S.; Seeger, R.; Pople, J. A. Self-consistent Molecular Orbital Methods. XX. A Basis Set for Correlated Wave Functions. *J. Chem. Phys.* **1980**, *72*, 650–654.

(35) Wehner, J.; Brombacher, L.; Brown, J.; Junghans, C.; Çaylak, O.; Khalak, Y.; Madhikar, P.; Tirimbò, G.; Baumeier, B. Electronic Excitations in Complex Molecular En-

vironments: Many-Body Green's Functions Theory in VOTCA-XTP. *J. Chem. Theory Comput.* **2018**, *14*, 6253–6268.

(36) Adamo, C.; Barone, V. Toward Reliable Density Functional Methods without Adjustable Parameters: The PBE0 Model. *J. Chem. Phys.* **1999**, *110*, 6158–6170.

(37) Hybertsen, M. S.; Louie, S. G. Electron Correlation in Semiconductors and Insulators: Band Gaps and Quasiparticle Energies. *Phys. Rev. B* **1986**, *34*, 5390–5413.

(38) Godby, R. W.; Needs, R. J. Metal-Insulator Transition in Kohn-Sham Theory and Quasiparticle Theory. *Phys. Rev. Lett.* **1989**, *62*, 1169–1172.

(39) Baumeier, B.; Rohlfing, M.; Andrienko, D. Electronic Excitations in Push–Pull Oligomers and Their Complexes with Fullerene from Many-Body Green's Functions Theory with Polarizable Embedding. *J. Chem. Theory. Comput.* **2014**, *10*, 3104–3110.

(40) Thole, B. T. Molecular polarizabilities calculated with a modified dipole interaction. *Chem. Phys.* **1981**, *59*, 341–350.

(41) Van Duijnen, P. T.; Swart, M. Molecular and atomic polarizabilities: Thole's model revisited. *J. Phys. Chem. A* **1998**, *102*, 2399–2407.

(42) Hush, N. S. Adiabatic Theory of Outer Sphere Electron-Transfer Reactions in Solution. *Trans. Faraday Soc.* **1961**, *57*, 557–580.

(43) Tirimbò, G.; Baumeier, B. Electronic Couplings and Conversion Dynamics between Localized and Charge Transfer Excitations from Many-Body Green's Functions Theory. *J. Chem. Theory Comput.* **2024**, *20*, 4605–4615.

(44) Butcher, J. *Numerical Methods for Ordinary Differential Equations*, second edition ed.; John Wiley & Sons Inc: New York, 2008.